Formation and emission mechanisms of Ag nanoclusters in the Ar matrix assembly cluster source

Junlei Zhao,[1] Lu Cao,[2] Richard E. Palmer,[2,3] Kai Nordlund,[1] and Flyura Djurabekova[1]

[1]*Department of Physics and Helsinki Institute of Physics, University of Helsinki, P.O. Box 43, FIN-00014 Helsinki, Finland*
[2]*Nanoscale Physics Research Laboratory, School of Physics and Astronomy, University of Birmingham, Birmingham B15 2TT, England, United Kingdom*
[3]*College of Engineering, Swansea University, Bay Campus, Fabian Way, Swansea SA1 8EN, Wales, United Kingdom*

In this paper, we study the mechanisms of growth of Ag nanoclusters in a solid Ar matrix and the emission of these nanoclusters from the matrix by a combination of experimental and theoretical methods. The molecular dynamics simulations show that the cluster growth mechanism can be described as "thermal spike-enhanced clustering" in multiple sequential ion impact events. We further show that experimentally observed large sputtered metal clusters cannot be formed by direct sputtering of Ag mixed in the Ar. Instead, we describe the mechanism of emission of the metal nanocluster that, at first, is formed in the cryogenic matrix due to multiple ion impacts, and then is emitted as a result of the simultaneous effects of interface boiling and spring force. We also develop an analytical model describing this size-dependent cluster emission. The model bridges the atomistic simulations and experimental time and length scales, and allows increasing the controllability of fast generation of nanoclusters in experiments with a high production rate.

I. INTRODUCTION

Arguably, the most prototypical nanoscience object possible is the single pure nanocluster. This is the structure that has quantum confinement in all three dimensions, and can be used to examine basic nanoscience effects [1–7]. Moreover, the extensive surface area to volume ratio in nanoclusters makes them attractive for catalytic and gas sensing industrial applications. New technologies based on the use of nanoclusters and nanoparticles are continually becoming available in contemporary industry [8–11]. The mass production of pure nanoclusters, however, is hindered by a low rate, which cannot be currently upscaled from the laboratory condition to industrial needs due to physical limitations.

Very pure nanoclusters can be synthesized in gas-phase condensation sources [12–15], which are known for a rather low production rate. Thus, mostly the current practical applications rely on nanoparticles made by chemical or lithographic means [16–18], as these can be produced efficiently on an industrial scale.

In our recently developed setup, the Matrix Assembly Cluster Source (MACS) [19–22], we demonstrate the possibility of scaling up of the production rate of nanoclusters via solid-state clustering. The method is based on the assembly of the metal clusters within a condensed gas matrix held at cryogenic temperatures, which are then sputtered by an Ar ion beam. The experiments show that the size of the obtained Au and Ag nanoclusters can be tuned from a few atoms to a few thousand atoms. However, from the experiments it is not clear what the fundamental physical processes underlying the new efficient cluster production process are, making further development and optimization of the process difficult.

To enable a controlled emission of large metal clusters from an Ar matrix, it is crucial to understand both how the clusters form within the matrix and how they are emitted from the matrix.

The sputtering phenomenon of metal or metal alloys (e.g., for thin-film growth) has been extensively studied both computationally and experimentally [23,24]. However, if a metal nanocluster is embedded in a gas condensed matrix, the process of sputtering may proceed differently. The main difference here is that the metal-inert gas matrix sputtering depends on (i) the cohesive energy of the solid gas; (ii) the cohesive energy of the metal; (iii) the concentration and distribution of the metal atoms inside the matrix due to initial metal load condition; (iv) the interaction between gas atoms and the metal atom; and (v) the temperature of the matrix. We note, in particular, that metals have much higher cohesive energies compared to an inert gas material such as Ar. This leads to sputtering yields of inert gas matrices several orders of magnitude higher than that of a metal target for the same impact energy [19,25]. Here we also note that there is another mechanism, which is known to enhance dramatically sputtering yields of materials. This is the so-called thermal (or heat) spike sputtering [26] from liquidlike regions of very high transient temperature ($\sim$10 000 K), which are induced in dense materials by energetic incoming ions [27–30]. If such a thermal spike develops near the surface, the sputtering yield can grow several orders of magnitude [31]. These short-lasting heat spikes may also cause major atom redistribution in the irradiated material [32].

In this paper, we use molecular dynamics (MD) simulations combined with analytical models to explain the efficient production of large metal nanoclusters, which we obtain in the MACS experimental setup. We study step by step the growth and distribution of Ag nanoclusters in the Ar matrix, as well as the subsequent emission of Ag nanoclusters from the Ar matrix. The processes considered were broken down into two stages: clustering and emission. Our simulations show that clustering of metal atoms enhanced by the thermal spike initiated in the Ag-rich Ar matrix by the incoming Ar ions is the predominant growth mechanism of Ag clusters. Moreover, we show that conventional sputtering mechanisms cannot explain

the formation of large clusters. Instead, their emission process proceeds by boiling of the interface between the Ag cluster and the matrix, and that a matrix spring-force effect completes the emission.

II. METHODS

A. Experiments

The experiments were carried out using the upgraded MACS developed at the University of Birmingham. The system is operated at UHV condition with a base pressure below 10^{-8} mbar. The key components include (a) the cooling system—a closed-cycle cryocooler providing the cooling power for the condensation of the matrix; (b) the evaporator—a high-temperature (up to 2000 °C) effusion cell (with a crucible size of 10 cc) to evaporate atoms of the cluster material into the matrix; (iii) the ion source and ion optics—a high flux ion source with maximum output current of 4 mA; and (iv) the (cooled) matrix condensation support—a 1 × 1-in. copper plate. The metal concentration in the matrix is determined from the evaporation flux (monitored by a quartz crystal microbalance) and Ar atom deposition rate (monitored by the gas pressure in the chamber). Clusters produced in the MACS are analyzed using an aberration-corrected scanning transmission electron microscope (STEM) (JEOL 2100F). The flux of clusters produced is obtained (by STEM) from the density of clusters deposited on the substrate within a certain time. The sizes of the clusters are measured from the integrated high angle annular dark field (HAADF) intensity compared with the HAADF intensity of single atoms as a reference.

B. Simulation

In the current paper, we have performed MD simulations aiming at two goals: (i) to understand the growth mechanism of Ag nanoclusters in the solid Ar matrix and (ii) to determine what mechanisms drive the emission of large individual Ag nanoclusters embedded in the matrix. To achieve the two goals, we performed two different kinds of simulations, which we denote **S1** and **S2**. In simulation type **S1**, we examined multiple subsequent Ar ion impacts on the cryogenic Ar matrix loaded with Ag atoms with different concentrations. Since formation of a single, individually positioned nanocluster is beyond the reach of a classical MD method, which was used in the current paper, we performed a series of simulations of a single Ar ion impact on the Ar matrix containing an individual Ag nanocluster to investigate the details of the emission mechanism (simulation type **S2**).

All simulations were conducted by using the classical MD code PARCAS [30,33]. We used the embedded atom method (EAM) potential [34,35] to model Ag-Ag interaction and the Lennard-Jones potential [36] to describe the Ar-Ar interactions. Both potentials reproduce the values of cohesive energies sufficiently close to experimental data [37]. To describe the Ar-Ag interaction, we used the pair potentials obtained directly from density functional theory calculations, according to the approach described in [38,39]. This approach gives both the high-energy repulsive and attractive part of the potential directly. For the Ar-Ag interaction, it gives a weak

van der Waals-type attraction, as expected for noble gas-metal interactions.

For the type **S1** multiple ion impact simulations, we constructed the simulation cell consisting of 512 000 atoms organized in the fcc lattice. The size of the simulation cells is about 208 × 208 × 416 Å initially. The three different simulation cells with the Ag loads of 5, 10, and 20 at. % were prepared as follows. The amount of Ar atoms corresponding to the given Ag load were replaced in the simulation cell by Ag atoms. All replaced atoms were selected at random uniformly to ensure the uniform Ag load of the Ar matrix. After that the system was relaxed in the isothermal-isobaric ensemble with periodic boundaries in all dimensions, at 10 K and zero pressure for 50 ps. The relaxation led to slightly modified cell dimensions depending on the load of Ag atoms. After that, the open surface on top and fixed atomic layers within 10 Å at the bottom allowed us to take into account the surface effects in the simulations. The bottom atoms were fixed to avoid the movement of the entire cell due to the momentum introduced by the incoming ion. The open surface was relaxed by running simulations in the canonical ensemble used for 10-Å thick layers right above the fixed bottom and the periodic boundaries in x and y dimensions for 15 ps.

For simulations of type **S2**, we prepared cells without an Ag load initially. For these simulations, we prepared an amorphous Ar structure in order to represent the Ar matrix amorphized by ion impacts. We heated the Ar crystal cell with periodic boundaries in all directions to the gas phase in the isothermal-isobaric ensemble at the pressure of 1 bar for 100 ps and then froze it back to 10 K at zero pressure. The final structure was completely amorphous with very small crystalline phases. After we opened the surface and performed additional relaxation as in the simulations **S1**, the size of the cell changed only negligibly due to surface relaxation only. This cell was used for the single ion impact simulations after the nanocluster was embedded in it. The size of this cell was 216.4 × 216.4 × 162.3 Å. In this cell of the pure Ar amorphous structure, we embedded Ag nanoclusters of three different sizes: 236, 466, 1024, and 2046 atoms, at the distance of 10 Å below the open surface, but in the middle of the cell in the lateral directions. After the nanocluster was inserted, the simulation cell was additionally relaxed during 100 ps. This cell was used for the single ion impact simulations after the nanocluster was embedded in it.

To simulate the interaction of energetic ions with the prepared matrices, we applied a standard technique used broadly in modeling of radiation effects in materials by MD methods [30,40]. These simulations are run in a quasimicrocanonical ensemble, to avoid the artifacts in the cascade development: the cascade is developed in the microcanonical (NVE) ensemble—no scaling of atom velocities is applied—however, in the narrow regions near the borders of the simulation cell, where atoms are not involved in the cascade, the temperature is controlled by applying the Berendsen thermostat [41]. In this manner, we can take into account the heat dissipation to the infinite bulk material. In our case, it was 15 Å from the border of the simulation box in the x and y directions and the atoms within 10 Å above the fixed bottom layers in the z direction. This sputtering simulation approach has been proven to give results closely comparable to the experiment [42].

To simulate ion impacts in simulation type **S1**, an Ar atom was initially placed at $(0, 0)$ position laterally, and at 8 Å above the highest point of the open surface with the fixed kinetic energy. The angle of incidence was set to be $7°$ off the normal to the surface. Each sputtering event was simulated for 150 ps. In multiple subsequent impact simulations, the simulation cell was shifted horizontally with a random vector (x, y) after each cascade to imitate a random position of entrance of the following ion. The sputtered atoms, which do not affect the cascade simulations, were removed from the simulation box.

In simulation type **S2**, i.e., nanocluster emission simulations, the statistical uncertainty was taken into account by running ten independent simulations with different initial velocities of the atoms in the cell and initial ion positions randomly selected at the distance of 8 Å from the surface within the circle of 10 Å in diameter above the nanocluster. The temperature was controlled only within the narrow regions near the borders as described above.

In our simulations, we have also used the binary collision approximation (BCA) code, CASWIN [43], which was modified to account for the required geometry of the embedded nanocrystals. In these simulations, the interaction between the incoming ion and amorphous matrix is calculated using the universal Ziegler-Biersack-Littmark (ZBL) repulsive potential [44]. Electronic stopping is implemented in the code similarly to the implementation in PARCAS as the function of the atom velocity, $dE/dx(v)$. The stopping was obtained from [45] and applied to the atoms with the energies greater than the cutoff energy ~ 5 eV. In these simulations, we placed Ag nanoclusters with different diameters (from 2 to 8 nm) right below the surface, to imitate the geometry assumed in the analytical model (see Sec. V). The Ar ions with the energy of 1 keV entered the surface of the matrix at the lateral center of the nanocluster. All the energy, which was transferred in nuclear collisions within the nanocluster below the displacement threshold, E_d, was recorded as the nuclear deposited energy. We also recorded all the electronic energy losses by the energetic atoms within the nanocluster. We note here that, in principle, the amount of the nuclear deposited energy should depend on the value of the displacement threshold E_d. However, we tested this in the reasonable range of values $E_d(Ag) = 15$–25 eV, and we did not find significant difference in the final temperature of the nanocluster, which is important for the conclusions of the present paper. Here we present only the results obtained with $E_d(Ag) = 25$ eV and $E_d(Ar) = 5$ eV. The results were averaged over 10 000 simulations for each case, with the error bar (standard error of the mean) not exceeding 1 eV.

III. EXPERIMENTS

The present experiments are designed to provide efficient emission of large nanoclusters from a solid matrix by ion sputtering. The MACS [19] is designed to produce efficiently large size Ag nanoclusters (tens of atoms upwards) by energetic ion sputtering of a cryogenic Ar (or slightly warmer CO_2 [20]) matrix, preloaded with metal atoms, in a reflection [21] or unconventional transmission geometry. An illustration of Ar^+ impacts in the applied geometry is shown in Fig. 1. The
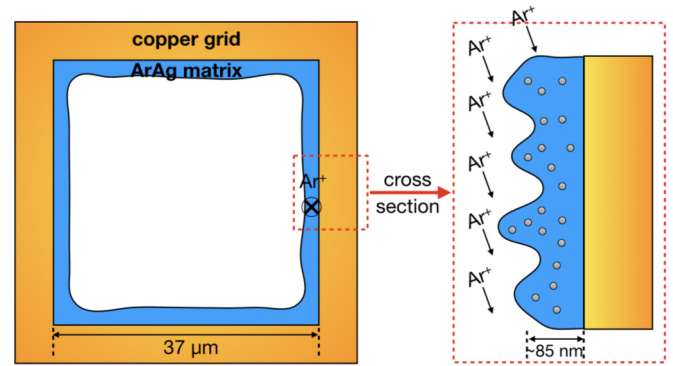

FIG. 1. Illustration of the grid geometry with respect to the ion-beam direction. On the right in the enlarged cross section, the condensed Ar matrix (shown in blue) is a thin layer on the inner side of the grid. The Ag atoms in the matrix are shown in a light gray color.

Ar matrix—which is only a thin layer on the inside of the holes in the Cu grid on which the Ar is condensed—is subjected to the Ar ion irradiation in the transmission regime in the present case. In this way, only the nanoclusters formed/located close to the rough surface can be emitted.

In the MACS source, the matrix is condensed on a support mounted on a closed-cycle cryocooler, while evaporation of Ag to load the matrix is performed in a high-temperature effusion cell. A quartz crystal microbalance in front of the evaporator allows for accurate control of dose rate to obtain well-defined metal concentrations. To drive the cluster formation and subsequent cluster emission, we used energetic Ar ions impacting on the cold Ar matrix. The ions were generated in a high flux ion source with a specially designed ion optical system to focus the ion flux onto the matrix.

The Ag clusters were deposited on amorphous carbon films and characterized by atom counting [46,47] in the aberration-corrected STEM, operating in HAADF mode. The images of the Ag clusters, which we obtained from the matrices with metal concentration ranging from 0.6 to 3.2 at. %, are shown in Figs. 2(a)–2(d). The insets show the atomic resolution of nanoclusters randomly selected from the corresponding sets of nanoclusters. The sizes of the clusters generated by the matrix and the deposition rate are plotted in Fig. 2(e) as a function of metal concentration. The size of a cluster is obtained from its integrated HAADF intensity compared with the HAADF intensity of single atoms on the same support. The cluster deposition rate (the total number of nanoclusters landed on the deposition substrate per unit time) is derived from the cluster density in the images. Figure 2 shows two main results: (i) the mean cluster size increases monotonically with metal concentration in the matrix and already exceeds 1000 atoms when the concentration is only $\sim 3\%$; (ii) the cluster deposition rate decreases monotonically as the metal concentration and cluster size increase. With regards to result i, we note that the sputtering yield of an Ar matrix subject to Ar ion sputtering at 1 keV is about 1000 atoms [25], so a homogeneous concentration of 3% metal atoms should yield a cluster only about 30 atoms in size in a single ion impact event, which is not consistent with the much larger clusters observed. This is why we turn to computer
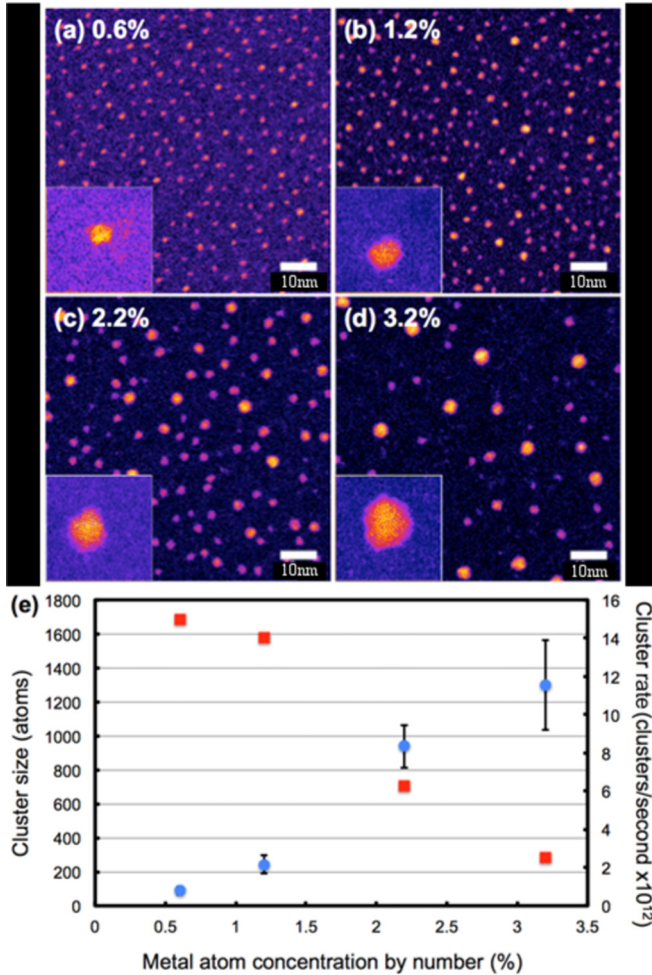
FIG. 2. (a–d) HAADF STEM images (2 M×) and (inset) atomic resolution images (12 M×) of Ag clusters prepared in the MACS with metal concentration in the matrix from 0.6 to 3.2 at. %. (e) A plot of cluster size (blue circles) and cluster intensity (rate) (red squares) as a function of metal concentration. Experimental parameters: matrix support, 1000 mesh copper grid; matrix temperature, 9 K; condens-xbrk ation time, 200 s; Ar gas dosing pressure, 6×10^{-8} mbar; matrix thickness, ∼85 nm; incident ion-beam current on matrix, 50 μA; ion-beam energy, 1 keV; deposition time from matrix, 120 s.

simulation to understand the key mechanisms leading to cluster growth and emission at cryogenic temperatures.

IV. SIMULATIONS

A. Thermal spike enhanced clustering

To determine the process by which Ag clusters can grow in an Ar matrix under ion bombardment, we first used simulation type **S1** to run 200 Ar ion irradiation events for each Ar matrix with 5, 10, and 20 at. % of Ag content. Since the Ag-rich Ar matrix is constantly kept at 10 K, the equilibrium diffusion process of Ag atoms cannot be expected to be the driving force of the segregation process. Our simulations show that in the cascades developed in the irradiated matrix the heat spikes develop where the temperature can be as high as 10 000 K, which is sufficient to induce the local boiling of Ar atoms.
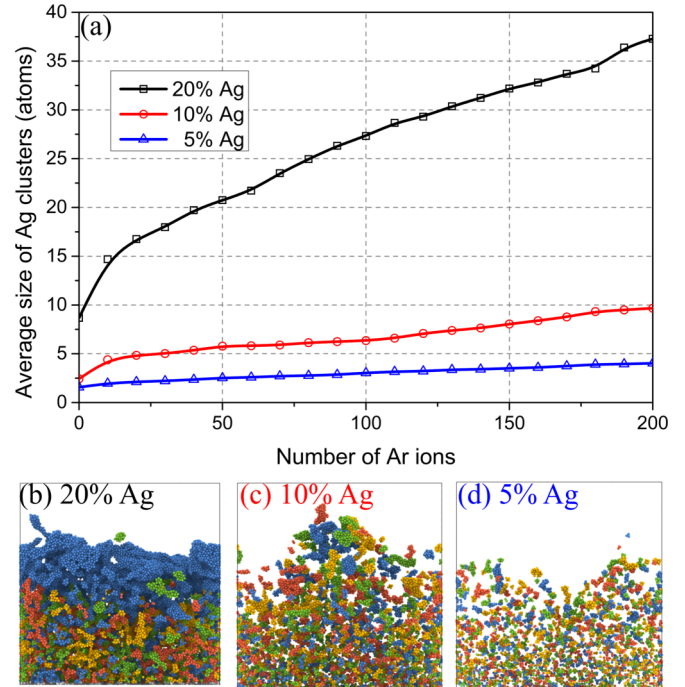

FIG. 3. (a) Evolution of the average size of Ag clusters agglomerated in the matrix as a function of the number of incoming Ar ions. The inset figure shows the detailed evolution for the 5- and 10-at. % Ag concentrations. (b–d) Simulation snapshots of the matrix with the different content of Ag atoms after 200 ion impacts. Four-color coding is used to distinguish separated clusters.

These heat spikes can enhance mobility of the Ag atoms in the Ar matrix. Since the Ag-Ag bond is about two orders of magnitude stronger than the Ar-Ar and Ar-Ag van der Waals bonds, any Ag atom that happens to meet another one in the random walk in the boiling Ar matrix within the heat spike is very likely to stay attached to it. This leads to the onset and growth of Ag clusters. Moreover, as shown in Fig. 3(a), the average size of the Ag clusters in all three matrices increases as a function of the number of sequential Ar ion impact events in the simulations. In the case of the 20-at. % Ag concentration, the growth saturates by the formation of a continuous foamlike network, as illustrated in Fig. 4(a). For the 5- and 10-at. % Ag concentrations, the cluster growth continues throughout the MD runs. For even larger numbers of incoming ions, corresponding to the experimental fluences, growth of large clusters can thus be expected.

By examining the ion impact events and the subsequent sputtering process closely, we found that most of the atomic clustering events indeed happened in or near the thermal spike. An example of a sputtering event is shown in Fig. 4(b) (see Supplemental Material, movie S1 [48]). In Fig. 4(b), the Ag atoms shown in cyan color are those which were displaced by more than 5 Å. As one can see, they all originated from the region near to the initial Ar ion impact point, shown as a blue open circle. The yellow lines show the trajectories of atoms from their original positions before the original impact. The temperature of the Ag atoms within the thermal spike is above the boiling point of the Ar matrix, but well below the melting point of the Ag cluster, so the small Ag clusters in the thermal
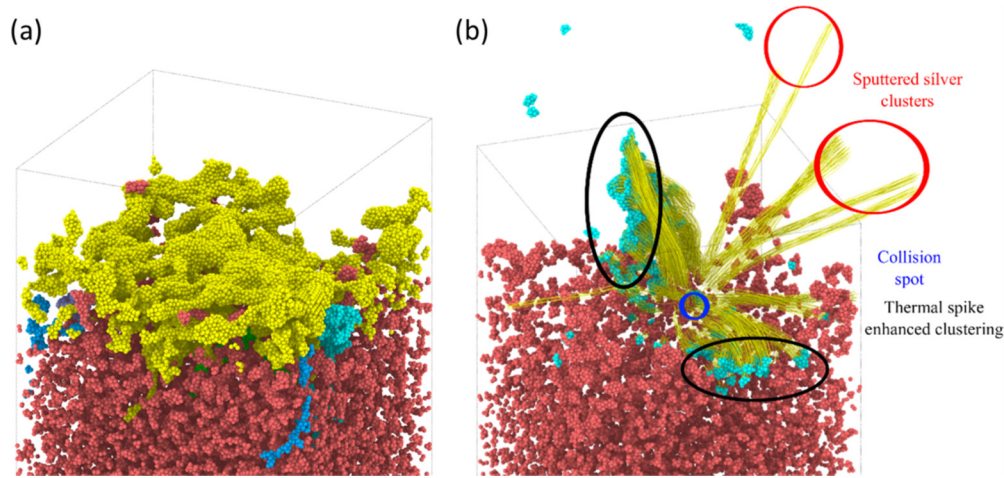
FIG. 4. (a) Final state after 200 ion irradiations for an Ar matrix loading with 20-at. % Ag atoms. Only Ag atoms are shown here. The Ag atoms clustered into a foamlike structure rather than individual clusters. The color coding in (a) shows several separated foams formed in the matrix. The largest one is shown in yellow. This fact can explain the decrease in sputtering yield for very heavy Ag loads. (b) An example of a sputtering event (for a 10-at. % Ag sample in an Ar matrix after 54 irradiations). The atoms which have more than 5-Å displacement during the sputtering are colored in cyan. The blue circle indicates the ion impact point. The black and red cycles show atomic clusters and individually sputtered small clusters up to 15 atoms, respectively. The yellow lines show the trajectories of each moving atom (see Supplemental Material, movie S1 [48]).

spike now have a chance to assemble into larger clusters in the liquid Ar matrix.

It is also worth noting that the production efficiency is not always positively correlated with the concentration of Ag in the matrix. The reason becomes obvious after examining the 20-at. % Ag sample after 200 impact events, as shown in Fig. 4(a). In the near-surface region of the matrix, upon the thermal spike clustering, a foamlike continuous Ag structure is formed. This structure will prevent further erosion by sputtering. As the sputtering yield of a pure Ag target responding to 1-keV Ar ion impact is less than 10 [24], only a cloud of Ag and Ar atoms will be emitted from this matrix. This also leads to the conclusion that the steady-state emission of Ag clusters requires that the Ag clusters must first grow within the matrix on a distance from one another and only after that be sputtered as a whole cluster.

To summarize the results from simulation type **S1**, atom motion enhanced by energetic-ion induced heat spikes can explain how metal clusters grow in an Ar matrix, but also that large metal clusters cannot be sputtered by a normal collision cascade mechanism. Hence we turn next to the question of how they can be emitted, using simulation type **S2**. Sputtering from dense nonlinear cascades (i.e., heat spikes) can also lead to cluster emission. However, the probability of cluster emission decreases strongly with cluster size [49–51], which is not consistent with the observations from the MACS experimental results. Hence we have to seek another mechanism of metal cluster emission in the MACS process.

B. Interface boiling and spring force effect

As we discussed in the previous section, for a large Ag cluster to be sputtered out of the matrix, it is necessary that the cluster is well isolated from the other surrounding Ag clusters. Sputtering from dense nonlinear cascades (i.e., heat spikes) can in principle lead to cluster emission. However, the

probability of cluster emission decreases strongly with cluster size [49–51], which is not consistent with the observations from the MACS experimental results. Hence we have to seek another mechanism of metal cluster emission in the MACS process.

Here we use simulation type **S2** with a model system of a single spherical Ag cluster embedded in the Ar matrix to study the emission mechanism. The Ag cluster, which would be produced in practice by multiple ion impact events, is placed about 1 nm below the Ar surface. As shown in Fig. 5, within the first 1 ps, after the collision the Ag cluster is melted and then rapidly cooled down below 1000 K. The process is illustrated in Fig. 6, by showing a series of cross sections of the simulation cell frames at several subsequent times. The results show that the Ag cluster detaches from the Ar matrix by boiling of the Ar layer at the interface with the metal cluster. Moreover, the momentum of the Ar ion is transferred to the Ag cluster, leading the entire cluster to gain a momentum directed towards the bulk of the matrix. This in turn will initially compress the matrix. This compression is released in the form of an elastic spring force, which brings the cluster back to the surface still in the warm state (hence not bound to the cryogenic matrix). Furthermore, the entire process of cluster emission from the matrix can occur only within a given time window, i.e., before the system freezes again. For a given sputtering energy, the average duration of the time window for the cluster detached from the matrix is dependent on the cluster size, the energy initially deposited into the cluster, and the initial depth of the cluster. Clusters smaller than the volume of the thermal spike are most likely to move towards the underdensified region of the thermal spike, and this effect may be stronger than the spring force. On the other hand, clusters which are too large will have a very short time window to "escape" from the matrix before the hole above the cluster is filled in by Ar atoms flowing back from the sides.
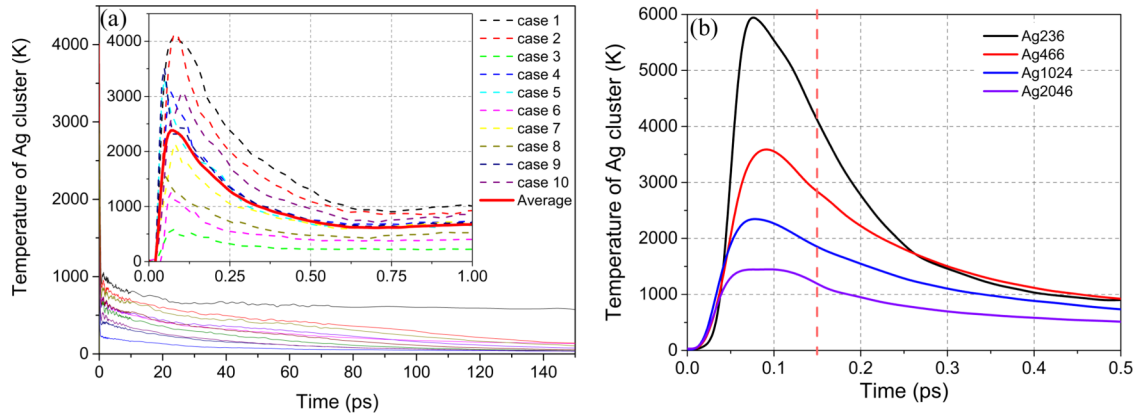
FIG. 5. (a) Ten cases of random Ar^+ ion impacts on a Ag_1024 cluster embedded in a solid Ar matrix (see Sec. II B for simulation detail). Evolution of the temperature of the Ag cluster in each case is plotted as a function of the simulation time. The kinetic energy of sputtered Ag atoms is not included. The inset shows the temperature evolution in the first 1 ps. After the collision the Ag cluster is heated up to 2400 K on average and then cools down to 1000 K within 1 ps. The labels of the axis of the inset graph are the same as the main graph. The Ag cluster with high kinetic energy boils the surrounding Ar atoms, providing a possible route to cluster detachment from the matrix surface (see Supplemental Material, movie S2 [48]). (b) The averaged temperature evolution of the different sized Ag clusters. The vertical red dashed line indicates the time frame (0.15 ps), which was selected for comparison of temperature of the nanoclusters with the analytical model [see Fig. 8(b)].

More simulations were performed for different sizes of Ag clusters: Ag_{236}, Ag_{466}, and Ag_{2046}. As shown in Fig. 5(b), the averaged temperature evolution curves [the same curve as the solid red line in Fig. 5(a)] are plotted for the first 0.5 ps. The plot shows that the initial temperature of the Ag clusters increases with decrease of the cluster size, while the cooling rate of the small clusters is also larger. However, the highly stochastic nature of the collision cascade processes prevents the use of MD simulations to derive statistically reliable conclusions about the interplay of these emission processes. Thus we further develop an analytical model to describe the process of cluster emission quantitatively.

V. ANALYTICAL MODEL OF EMISSION

In order to describe the cluster emission process as a function of the cluster size, we develop an analytical model to predict the duration of boiling of the interface. A schematic illustration of the model is shown in Fig. 7. The whole process can be broken down into two parts: energy deposition and thermal transmission. The form of the distribution of the energy deposited by the Ar ion into the matrix is considered as Gaussian [52,53]:

$$\varepsilon(x,y,z) = \frac{E_{\text{eff}}}{2\pi^{3/2}a^2b} \exp\left(-\frac{x^2+y^2}{2a^2}\right) \exp\left(-\frac{z^2}{2b^2}\right)$$
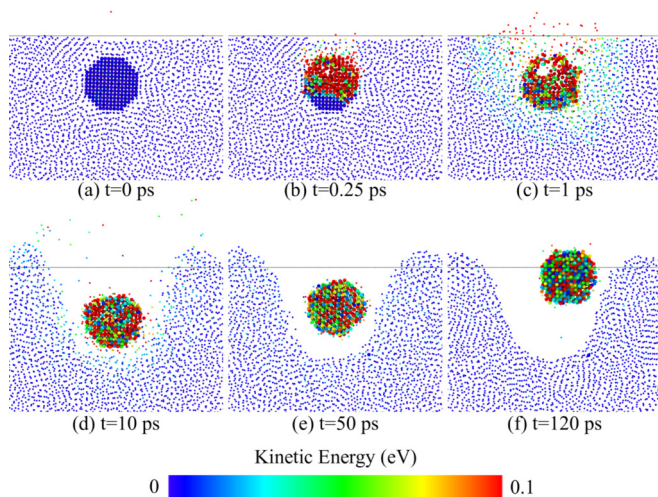
(1)

FIG. 6. Two-dimensional sliced cross section of case 1 in Fig. 5. The Ag and Ar atoms are shown as large and small circles, respectively. The color coding shows the kinetic energy from 0 to 0.1 eV (see Supplemental Material, movie S2 [48]).
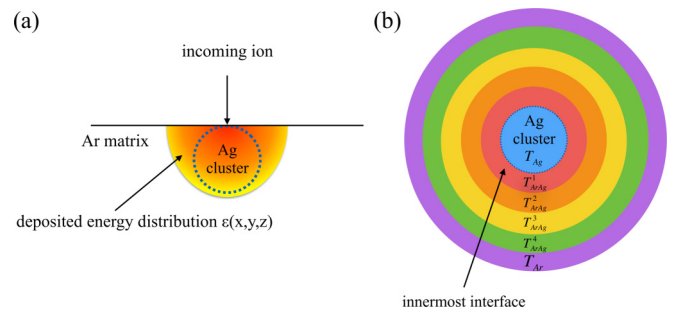

FIG. 7. A schematic illustration of the analytical model. (a) Energy deposition: The Ag cluster (the dashed-line circle) is placed right below the surface of the Ar matrix. The shape of the distribution of the deposited energy is a Gaussian hemi-ellipsoid (orange region). The ion impact point and origin of the distribution are at the center of the cross section of the cluster and at the surface of the matrix. (b) Thermal transmission: The Ag cluster is surrounded by the Ar matrix. The temperature evolution of five layers of the Ar/Ag interface is calculated.
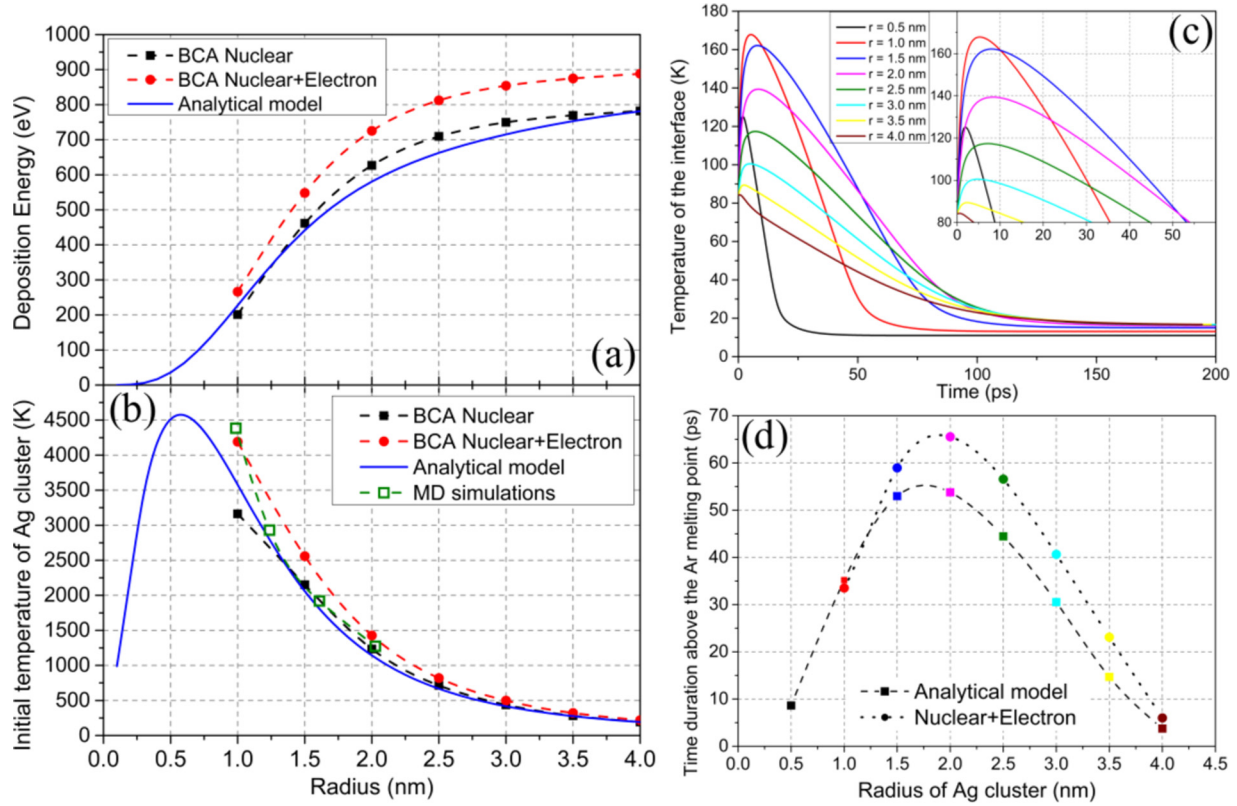
FIG. 8. (a) Energy deposited E_p and (b) initial temperature as functions of the radius of the Ag cluster. The blue curve is the analytical model [see Eq. (3)]. Red and black dashed curves are calculated in binary collision approximation (CASWIN [43]) with and without taking into account the electronic stopping power, respectively. The green dashed curve shows the MD simulation results plotted using the data in Fig. 4(b) at 0.15 ps. (c) Temperature evolution of the interface (innermost layer) T_{ArAg}^1. The inset shows the time interval while the interface temperature is above the melting point of Ar. (d) Time intervals while the cluster-matrix interface is in the liquid phase as a function of the size of the Ag cluster. Two different initial conditions are calculated with analytical and BCA models. The color code of the points plotted corresponds to the color coding used in (c).

where E_{eff} is the effective deposited energy which is fitted from the Gaussian distribution. Since the distribution of the deposited energy has a hemiellipsoid shape, E_{eff} is two times greater than the energy of the ion. a and b are the standard deviations in lateral (x and y) and perpendicular to the surface (z) directions, respectively. Here we assume that $a = b$ for the low ion energy region, where cascades are roughly spherical. We use

$$a = b = \alpha_{\mathrm{Ar}} - \frac{\alpha_{\mathrm{Ar}} - \alpha_{\mathrm{Ag}}}{\exp\left(-\frac{\sqrt{\sum_{x,y,z}(i-i_c)^2}-r}{\mu}\right) + 1} \qquad (2)$$

where α_{Ar} and α_{Ag} are the standard deviation of the deposited energy distribution in pure Ar and Ag target, respectively; these are fitted to binary collision approximation the Transport of Ions in Matter (TRIM) simulations [45] with 10^6 irradiation events. For a 1-keV Ar ion, the values of α_{Ag} and α_{Ar} are 10.4 and 47.4 Å, respectively. In order to have a smooth transition from α_{Ag} to α_{Ar} at the Ag-Ar interface, we describe the transition region as a Fermi-Dirac-like function. i_c represents the three-dimensional coordinates of the center of the cluster, (x_c, y_c, z_c), and i represents the coordinates of a given point in the matrix. μ is a fitted parameter to describe how sharp the transition is.

From Eqs. (1) and (2), one can obtain the total deposited energy by integrating over the cluster volume V:

$$E_p = \int_V \varepsilon(x,y,z)\,dV. \qquad (3)$$

We can then derive the initial temperature of the clusters, $T_{\mathrm{Ag}}(r,t_0) = E_p/(3Nk_B)$, as shown in Figs. 8(a) and 8(b), where $N = (\frac{4}{3}\pi r^3)/\overline{V}$ is the number of Ag atoms, $\overline{V}$ being the average volume of a Ag atom. We also compare this analytical model with the classical BCA code CASWIN [43] implemented for the nanocluster geometry. The BCA approach allows for a much more efficient way of calculating the initial energy deposition profile during ion irradiation than MD, and thus enables us to obtain very good statistics. As shown in Figs. 8(a) and 8(b), the deposited energy and initial temperature are in a good agreement between the two methods. The increase of the cluster size allows for more energy to be received by the nanocluster directly, this is why the curve in Fig. 8(a) is rapidly increasing. However, it tends to saturate when the size of the developing cascade becomes comparable to the size of the nanocluster. The fast heat conduction inside the metal nanocluster allows for the assumption that the deposited energy becomes uniformly distributed within the cluster practically instantaneously. Therefore, knowing

the deposited energy within the Ag nanocluster, we can estimate its initial temperature, which rapidly decreases from 1.0- to 4.0-nm radius, as shown in Fig. 8(b).

From the initial temperature of the Ag atoms, we can further calculate the temperature evolution of the interface based on a series of differential equations describing the thermal flow:

$$\frac{dT_{\mathrm{Ag}}}{dt} = -\frac{\lambda^1_{\mathrm{ArAg}}\left(T_{\mathrm{Ag}} - T^1_{\mathrm{ArAg}}\right)(4\pi r^2)}{3dN_{\mathrm{Ag}}k_B}$$

$$\frac{dT^n_{\mathrm{ArAg}}}{dt} = \frac{\lambda^n_{\mathrm{ArAg}}\left(T^{n-1}_{\mathrm{ArAg}} - T^n_{\mathrm{ArAg}}\right)4\pi[r + (n-1)d]^2 - \lambda^{n+1}_{\mathrm{ArAg}}\left(T^n_{\mathrm{ArAg}} - T^{n+1}_{\mathrm{ArAg}}\right)4\pi(r + nd)^2}{3dN^n_{\mathrm{ArAg}}k_B} \tag{4}$$

$$\frac{dT_{\mathrm{Ar}}}{dt} = \frac{\lambda_{\mathrm{Ar}}\left(T^4_{\mathrm{ArAg}} - T_{\mathrm{Ar}}\right)4\pi(r + 4d)^2}{3DN_{\mathrm{Ar}}k_B}$$

where T_{Ag}, T^n_{ArAg}, and T_{Ar} are the temperatures of the Ag cluster, and the superscript n denotes the nth layer of interfaces ($n = 1, 2, 3$ in our system of equations) and the Ar matrix [see Fig. 7(b)]. The distance $d = 1$ nm is the thickness of layers and $D = 10$ nm is the thickness of the outermost Ar matrix. N_X is the number of atoms of type X in the corresponding layer. It is known that the thermal conductivity, λ, of solid Ar depends on the temperature, which can be fitted from the simulation data [54]. As shown in Fig. 8(c), the temperature of the innermost interface between the Ag cluster and Ar matrix [T^1_{ArAg} in Eq. (4)] evolves differently depending on the size of the clusters. The physics behind this can be explained by the balance between the initial temperature of the cluster and the interface area. A larger cluster receives a higher total deposited energy, but it also has a much larger interface area which promotes cooling. On the other hand, a small cluster with extremely high initial temperature will cool down fast by the surrounding matrix and mainly follow the thermal spike movement. Therefore, only medium sized clusters, around 1.5–2.0 nm in radius (3–4 nm in diameter), have the suitable ratio of sufficiently high deposited energy and total area of the interface to enable their sputtering. As shown in Fig. 8(d), with 1-keV ion energy, the maximum duration for the temperature of the interface to stay above the boiling point of the Ar matrix is reached if the size of the cluster is around 2 nm in radius.

VI. CONCLUSION

In this paper, we have explored the formation and emission mechanisms of Ag clusters from an Ar matrix under Ar ion bombardment. Using molecular dynamics simulations we have shown how atom motion in a sequence of thermal spikes generated by Ar 1-keV ion impact can explain the growth of Ag clusters in the Ar matrix. Furthermore, we have demonstrated that an interface boiling mechanism can explain why cluster emission occurs preferentially around a certain size range. We also developed an analytical model to describe the size dependence of the cluster emission to serve as a guide for the experimental studies. The model indicates that the most probable size of the emitted cluster depends on the balance of the deposited energy and the interface area. The mechanisms discussed in this paper are not specific for the Ag-Ar system only, and can be applied to a wide range of solid-phase gas-metal systems, and understanding these promises to contribute to the use of cluster beam sources for efficient technological applications.

[1] I. Lee, F. Delbecq, R. Morales, M. A. Albiter, and F. Zaera, Nat. Mater. **8**, 132 (2009).

[2] K. An and G. A. Somorjai, Chem. Cat. Chem. **4**, 1512 (2012).

[3] S. Syrenova, C. Wadell, F. A. Nugroho, T. A. Gschneidtner, Y. A. D. Fernandez, G. Nalin, D. Świtlik, F. Westerlund, T. J. Antosiewicz, V. P. Zhdanov *et al.*, Nat. Mater. **14**, 1236 (2015).

[4] G. Y. Tonga, K. Saha, and V. M. Rotello, Adv. Mater. **26**, 359 (2014).

[5] H. A. Atwater and A. Polman, Nat. Mater. **9**, 205 (2010).

[6] S. Linic, U. Aslam, C. Boerigter, and M. Morabito, Nat. Mater. **14**, 567 (2015).

[7] A. Gurlo, Nanoscale **3**, 154 (2011).

[8] C.-C. Wang, Y.-K. Chiou, C.-H. Chang, J.-Y. Tseng, L.-J. Wu, C.-Y. Chen, and T.-B. Wu, J. Phys. D **40**, 1673 (2007).

[9] Z. Nie, A. Petukhova, and E. Kumacheva, Nat. Nanotechnol. **5**, 15 (2010).

[10] S. Bose, C. Lawrence, Z. Liu, K. Makarenko, R. Van Damme, H. Broersma, and W. Van Der Wiel, Nat. Nanotechnol. **10**, 1048 (2015).

[11] P. D. Howes, R. Chandrawati, and M. M. Stevens, Science **346**, 1247390 (2014).

[12] O. F. Hagena, Rev. Sci. Instrum. **63**, 2374 (1992).

[13] P. Grammatikopoulos, S. Steinhauer, J. Vernieres, V. Singh, and M. Sowwan, Adv. Phys. X **1**, 81 (2016).

[14] S. Pratontep, S. Carroll, C. Xirouchaki, M. Streun, and R. Palmer, Rev. Sci. Instrum. **76**, 045103 (2005).

[15] D. Llamosa Perez, L. Martínez, and Y. Huttel, Dataset Papers in Science **2014**, 584391 (2014).

[16] T. Hyeon, Chem. Commun. **8**, 927 (2003).

[17] T. K. Sau and A. L. Rogach, Adv. Mater. **22**, 1781 (2010).

[18] Y. Sun and Y. Xia, Science **298**, 2176 (2002).

[19] R. Palmer, L. Cao, and F. Yin, Rev. Sci. Instrum. **87**, 046103 (2016).

[20] V. Oiko, T. Mathieu, L. Cao, J. Liu, and R. Palmer, J. Chem. Phys. **145**, 166101 (2016).

[21] P. R. Ellis, C. M. Brown, P. T. Bishop, J. Yin, K. Cooke, W. D. Terry, J. Liu, F. Yin, and R. E. Palmer, Faraday Discuss. **188**, 39 (2016).

[22] R. Cai, N. Jian, S. Murphy, K. Bauer, and R. E. Palmer, APL Materials **5**, 053405 (2017).

[23] *Sputtering by Particle Bombardment: Experiments and Computer Calculations from Threshold to Mev Energies*, edited by R. Behrisch and W. Eckstein (Springer, Berlin, 2007).

[24] M. Seah, Thin Solid Films **81**, 279 (1981).

[25] J. Schou, Nucl. Instrum. Meth. B **27**, 188 (1987).

[26] R. S. Averback and T. Diaz de la Rubia, in *Solid State Physics*, Vol. 51, edited by H. Ehrenfest and F. Spaepen (Academic, New York, 1998), pp. 281–402.

[27] F. Seitz and J. S. Koehler, Solid State Phys.-Adv. Res. Appl. **2**, 305 (1956).

[28] H. M. Urbassek and K. T. Waldeer, Phys. Rev. Lett. **67**, 105 (1991).

[29] T. Diaz de la Rubia, R. S. Averback, R. Benedek, and W. E. King, Phys. Rev. Lett. **59**, 1930 (1987).

[30] K. Nordlund, M. Ghaly, R. S. Averback, M. Caturla, T. Diaz de la Rubia, and J. Tarus, Phys. Rev. B **57**, 7556 (1998).

[31] A. Ilinov, A. Kuronen, K. Nordlund, G. Greaves, J. A. Hinks, P. Busby, N. J. Mellors, and S. E. Donnelly, Nucl. Instr. Meth. Phys. Res. B **341**, 17 (2014).

[32] K. Nordlund, L. Wei, Y. Zhong, and R. S. Averback, Phys. Rev. B (Rapid Comm.) **57**, R13965 (1998).

[33] K. Nordlund and R. S. Averback, Phys. Rev. B **59**, 20 (1999).

[34] S. M. Foiles, M. I. Baskes, and M. S. Daw, Phys. Rev. B **33**, 7983 (1986); **37**, 10378E (1988).

[35] S. M. Foiles and J. B. Adams, Phys. Rev. B **40**, 5909 (1989).

[36] J. E. Jones, Proc. R. Soc. A **106**, 463 (1924).

[37] C. Kittel, *Introduction to Solid State Physics* (Wiley, New York, 2005).

[38] B. Delley, J. Chem. Phys. **92**, 508 (1990).

[39] K. Nordlund, N. Runeberg, and D. Sundholm, Nucl. Instr. Meth. Phys. Res. B **132**, 45 (1997).

[40] M. Ghaly, K. Nordlund, and R. S. Averback, Phil. Mag. A **79**, 795 (1999).

[41] H. J. C. Berendsen, J. P. M. Postma, W. F. van Gunsteren, A. DiNola, and J. R. Haak, J. Chem. Phys. **81**, 3684 (1984).

[42] J. Samela, J. Kotakoski, K. Nordlund, and J. Keinonen, Nucl. Instr. Meth. Phys. Res. B **239**, 331 (2005).

[43] T. S. Pugacheva, F. G. Djurabekova, and S. K. Valiev, Nucl. Instr. Meth. Phys. Res. B **141**, 99 (1998).

[44] J. F. Ziegler, J. P. Biersack, and U. Littmark, *The Stopping and Range of Ions in Matter* (Pergamon, New York, 1985).

[45] J. F. Ziegler, J. P. Biersack, and M. D. Ziegler, *SRIM: The Stopping and Range of Ions in Matter* (Cadence Design Systems, Raleigh, NC, 2008).

[46] N. P. Young, Z. Y. Li, Y. Chen, S. Palomba, M. Di Vece, and R. E. Palmer, Phys. Rev. Lett. **101**, 246103 (2008).

[47] N. Jian, C. Stapelfeldt, K.-J. Hu, M. Fröba, and R. E. Palmer, Nanoscale **7**, 885 (2015).

[48] See Supplemental Material at http://link.aps.org/supplemental/10.1103/PhysRevMaterials.1.066002 for full movies.

[49] H. M. Urbassek, Nucl. Instr. Meth. Phys. Res. B **31**, 541 (1988).

[50] A. Wucher and B. J. Garrison, J. Chem. Phys. **105**, 5999 (1996).

[51] K. O. E. Henriksson, K. Nordlund, and J. Keinonen, Phys. Rev. B **71**, 014117 (2005).

[52] T. T. Järvi, J. A. Pakarinen, A. Kuronen, and K. Nordlund, Europhys. Lett. **82**, 26002 (2008).

[53] P. Sigmund, Phys. Rev. **184**, 383 (1969).

[54] K. V. Tretiakov and S. Scandolo, J. Chem. Phys. **120**, 3765 (2004).